nature climate change

Article

https://doi.org/10.1038/s41558-024-01956-w

Enhanced CO_2 uptake of the coastal ocean is dominated by biological carbon fixation

Received: 12 May 2023

Accepted: 14 February 2024

Published online: 22 March 2024

Check for updates

Moritz Mathis[1] ✉, Fabrice Lacroix[2,3], Stefan Hagemann[1], David Marcolino Nielsen[4], Tatiana Ilyina[4] & Corinna Schrum[1,5]

Observational reconstructions indicate a contemporary increase in coastal ocean CO_2 uptake. However, the mechanisms and their relative importance in driving this globally intensifying absorption remain unclear. Here we integrate coastal carbon dynamics in a global model via regional grid refinement and enhanced process representation. We find that the increasing coastal CO_2 sink is primarily driven by biological responses to climate-induced changes in circulation (36%) and increasing riverine nutrient loads (23%), together exceeding the ocean CO_2 solubility pump (41%). The riverine impact is mediated by enhanced export of organic carbon across the shelf break, thereby adding to the carbon enrichment of the open ocean. The contribution of biological carbon fixation increases as the seawater capacity to hold CO_2 decreases under continuous climate change and ocean acidification. Our seamless coastal ocean integration advances carbon cycle model realism, which is relevant for addressing impacts of climate change mitigation efforts.

The coastal ocean is a disproportionate sink for atmospheric CO_2, with shelf and marginal seas covering only ~7% of the world's ocean surface but taking up more CO_2 per area than the open ocean[1–4]. According to observational products, the global coastal ocean is currently absorbing 0.19–0.30 GtC yr^{-1} of CO_2 from the atmosphere (excluding estuaries and intertidal wetlands)[2–6]. Moreover, reconstructions of global ocean CO_2 partial pressure (p_{CO_2}) suggest that while both the open and coastal ocean CO_2 sinks have been increasing during the last decades, a faster increase in ocean–atmosphere p_{CO_2} gradients (Δp_{CO_2}) is occurring in the coastal ocean[7]. Estimates from conceptual and dynamical modelling, however, disagree due to simplifications and assumptions regarding process representation and spatio-temporal heterogeneity in coastal carbon fluxes[6]. The roles that terrestrial, atmospheric and open ocean drivers have in explaining the globally intensifying CO_2 absorption by coastal waters remain enigmatic, especially in quantitative terms. Recent global carbon budgeting studies highlight that ocean margins and land–ocean transition zones are critical areas where further research is needed to improve ocean carbon sink estimates[4,6,8,9].

Carbon dynamics in the coastal ocean are affected by a multitude of drivers that ultimately influence the magnitude of the coastal CO_2 sink. The equilibration of sea waters to increasing atmospheric p_{CO_2} levels and climate-induced changes in circulation affect the physical carbon export to the open ocean, raising the question of whether lateral off-shelf transport still induces a notable reduction in oceanic p_{CO_2} or whether this contribution is becoming negligible[7,10]. Agricultural fertilization and wastewater treatment have affected nutrient inputs from land, which in turn promote biological carbon fixation in the coastal ocean[11]. This raises the question of whether the additional biological carbon sequestration, under the influences of riverine freshwater and terrestrial carbon supplies on surface p_{CO_2}, can substantially slow down the accumulation of dissolved inorganic carbon (DIC) in coastal waters, thus enhancing the uptake of CO_2 from the atmosphere. Furthermore, enhanced stratification due to atmospheric warming weakens the vertical nutrient supply for biological productivity[12], lower CO_2 solubility of warmer water masses is associated with higher p_{CO_2} (ref. 13), and increasing sea water temperature reduces its CO_2 buffer capacity[14], limiting further absorption of CO_2 from the atmosphere.

[1]Institute of Coastal Systems, Helmholtz-Zentrum Hereon, Geesthacht, Germany. [2]Climate and Environmental Physics, University of Bern, Bern, Switzerland. [3]Oeschger Centre for Climate Change Research, University of Bern, Bern, Switzerland. [4]Max-Planck-Institute for Meteorology, Hamburg, Germany. [5]Institute of Oceanography, University of Hamburg, Hamburg, Germany. ✉e-mail: moritz.mathis@hereon.de

Table 1 | Overview of the conducted ICON-Coast simulations with further information on the prescribed atmospheric p_{CO_2}, meteorological forcing fields and riverine nutrient loads

Experiment	Period	Atmospheric p_{CO_2}	Meteorological forcing	Riverine nutrient loads
ctrl:	211 yr	constant 296 ppm	looped 1900–1919	looped 1900–1919
Control run		(year 1900)		
hist:	1900–2010	transient	transient	linear increase
Full hindcast run		(1900–2010)	(1900–2010)	
woriv:	1900–2010	transient	transient	looped 1900–1919
hist without increasing nutrient inputs from land		(1900–2010)	(1900–2010)	
hist$_{ext}$:	100 yr	constant 390 ppm	looped 1991–2010	looped 1991–2010
Continuation of hist with constant atmospheric p_{CO_2}		(year 2010)		
woriv$_{ext}$:	100 yr	constant 390 ppm	looped 1991–2010	looped 1900–1919
Continuation of woriv with constant atmospheric p_{CO_2}		(year 2010)		
woriv$_{inc}$:	40 yr	transient RCP8.5	looped 1991–2010	looped 1900–1919
Continuation of woriv with increasing atmospheric p_{CO_2}		(2011–2050)		

A looped forcing means that forcing conditions of a limited subperiod is continuously repeated over the whole model integration time to keep long-term conditions stable while still maintaining natural high-frequency variations. In contrast, a transient forcing means that forcing conditions follow their own specific temporal evolution over the model integration. See Extended Data Fig. 2 for further information on the prescribed atmospheric p_{CO_2} and the 'Experiment design' section for more details.

Observation-based studies on coastal ocean carbon fluxes are fraught with large uncertainty due to general data scarcity. In particular, the detection of long-term trends is impeded by high natural variability of biogeochemical transformation and exchange fluxes[4,15–17]. Global dynamic modelling approaches, by contrast, provide spatially and temporally complete variable fields but struggle to represent physical and biogeochemical processes relevant to the coastal carbon cycle, and their current coarse resolutions do not capture distinct regional circulation features[10,11,18,19].

Here we apply the global ocean-biogeochemistry model ICON-Coast[20] to derive a quantitative understanding of anthropogenic alterations in the CO_2 uptake efficiency of the coastal ocean. ICON-Coast adds value to coastal carbon modelling (exemplified in Extended Data Fig. 1) by applying an unstructured grid configuration with increased horizontal resolution in coastal areas and an extended representation of physical and biogeochemical processes to better account for shelf-specific carbon transformation, transport and storage dynamics. Particularly, ICON-Coast incorporates tidal currents including bottom drag effects and explicitly accounts for sediment resuspension, temperature-dependent remineralization and dissolution in the water column and sediment, riverine matter fluxes from land including terrestrial organic carbon, and variable sinking speed of aggregated particulate matter. With this approach, the model provides a seamless representation of the global marine carbon cycle, including two-way exchange between flows of the open ocean and the biologically productive coastal areas.

We conducted simulations over the historical period 1900–2010, which consider atmospheric changes in climate, increasing atmospheric CO_2 concentrations and the increase in anthropogenic nutrient inputs from land (Table 1 and Extended Data Fig. 2). On continental shelves and in the transition zone to the adjacent open ocean, the grid resolution is 20 km, which is 2–4 times finer than what could be achieved by earlier studies[10,11]. We investigate to what extent the processes controlling net carbon fixation in the coastal ocean can keep up with the rapidly rising p_{CO_2} in the atmosphere, thus contributing to an efficient CO_2 transfer from the atmosphere to the global ocean. We quantify the coastal carbon budget and identify key drivers altering burial, transport and air–sea gas exchange during the twentieth century.

Trends in global ocean CO_2 uptake

The ocean–atmosphere CO_2 flux (F_{CO_2}) shows a clear change towards a stronger net CO_2 sink over the 1900–2010 period (more negative F_{CO_2} in Fig. 1). This tendency holds for both the open and coastal ocean, and reflects changes in Δp_{CO_2} (Extended Data Fig. 3). Since the 1950s, Δp_{CO_2} increases by 0.20 ppm yr^{-1} in the coastal ocean, outweighing the 0.10 ppm yr^{-1} increase in the open ocean (linear trend, $P < 0.01$). The stronger signal in the coastal ocean is in line with the observational study of ref. 7. In our simulations, however, the increase rates are generally weaker by factors of 2 and 4 in the open and coastal ocean, respectively, and remain weaker when comparing to the same temporal period (winter trends since the 1980s) and spatial coverage (excluding Arctic and south-east Asian shelves). Yet, the trends derived in ref. 7 show substantial uncertainty, as the spreads (2σ) in their station-based data are 10 and 4 times larger than the corresponding globally averaged values. This high uncertainty is further underlined by the study of ref. 17, which utilized an early version of the SOCAT atlas[21] but did not find a notable trend in coastal Δp_{CO_2}.

The spatial distribution of the simulated Δp_{CO_2} signal (Fig. 2) mirrors the general trend in a downward flux direction, owing to predominantly lower p_{CO_2} increase rates in the ocean than in the atmosphere (represented by a negative change in Δp_{CO_2}). Exceptions are found mainly in the Southern Ocean and on Arctic shelves, where surface warming (by up to 1.4 °C) induces Δp_{CO_2} changes in the opposite direction. On a global average, the resulting net CO_2 uptake has a generally higher density (by 30–40%) in the coastal ocean than in the open ocean (Fig. 1).

The coastal ocean as a zone of carbon transformation

The coastal ocean is an area of high biological activity. Integrated net primary production (NPP) is simulated to be 5.1 PgC yr^{-1} for 1991–2010 (hist), or 11% of global marine NPP. The majority of this biogenically bound carbon is remineralized again on the continental shelves (87%). Of the remaining particulate organic and inorganic carbon, 224 TgC yr^{-1} gets buried in the shelf sediments, whereas 790 TgC yr^{-1} of dissolved (DOC) and particulate organic carbon (POC) is advected off-shelf to the open ocean (Fig. 3). As these export fluxes exceed the net import of 697 TgC yr^{-1}

https://doi.org/10.1038/s41558-024-01956-w

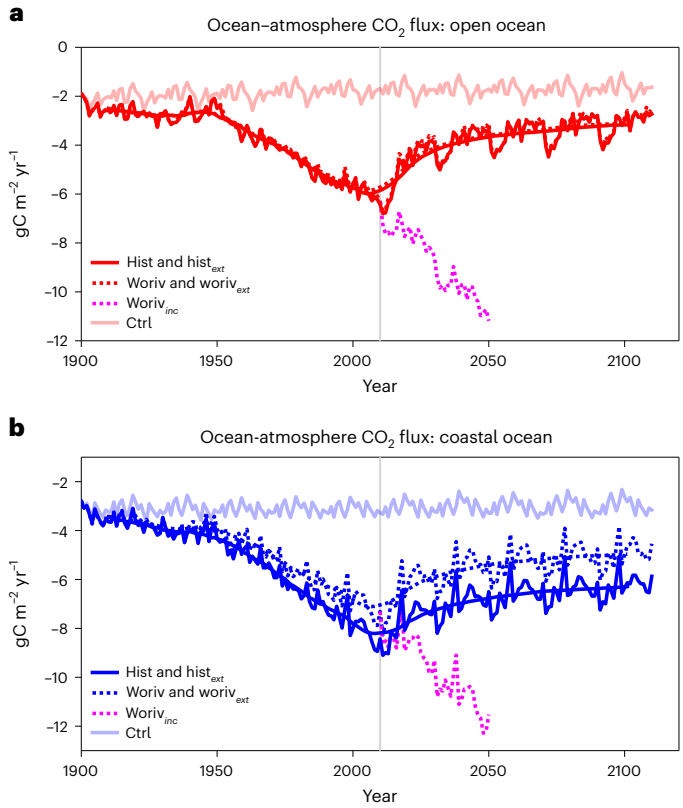

Fig. 1 | Time series of simulated ocean–atmosphere CO_2 flux density. **a**,**b**, Averages over the open (**a**) and the coastal (**b**) ocean. Both simulations woriv and hist of the period 1900–2010 were extended for another 100 years by constant atmospheric p_{CO_2} of the year 2010 (hist$_{ext}$ and woriv$_{ext}$, respectively), whereas woriv was additionaly extended for 40 years by continuously increasing atmospheric p_{CO_2} following emission scenario RCP8.5 (woriv$_{inc}$). Except for atmospheric p_{CO_2}, the extended runs were driven by looped forcings of the period 1991–2010 (see 'Experiment design'). The grey vertical line marks the transition to the extended runs. A negative sign indicates CO_2 flux into the ocean.

via rivers and 125 TgC yr^{-1} DIC via open ocean water masses, the resulting carbon deficit in coastal waters is balanced by net CO_2 uptake of 241 TgC yr^{-1} from the atmosphere. The coastal ocean thus shapes the marine carbon cycle by transforming inorganic carbon (IC) supplied by the land, atmosphere and open ocean into organic carbon (OC).

The net transformation of IC to OC in the coastal ocean is already simulated from the beginning of the twentieth century (ctrl), with a weak net uptake of atmospheric CO_2 of 95 TgC yr^{-1} (Fig. 3). This early coastal carbon sink confirms first evaluations of the preindustrial ocean state[4,22], which suggest a weak coastal CO_2 uptake of 40 and 100 TgC yr^{-1} for refs. 4 and 22, respectively, despite a net CO_2 release from the global ocean. According to our simulations, the cumulative anthropogenic impact during the twentieth century leads to more than a doubling of the coastal ocean CO_2 sink. By assuming that the off-shelf transport of POC is passed to the deep ocean and 20% of the DOC transport is removed from the upper ocean via new export production[23], we can verify the carbon reservoirs where the additionally absorbed CO_2 remains: 21% resides in shelf waters, 13% gets buried in shelf sediments, 44% is exported to the upper open ocean and 22% is transferred to the deep ocean.

Controls of the increasing CO_2 sink of the coastal ocean

The coastal CO_2 sink is enhanced by increased upwelling in the highly productive eastern boundary upwelling systems (EBUS) and by sea ice retreat in high latitudes, both caused by human-induced changes to the physical climate.

Changes in the near-surface wind pattern (Supplementary Fig. 1) reflect a global poleward migration of the large-scale atmospheric high-pressure fields, termed tropical expansion[24–26]. In the adjacent coastal EBUS of the Pacific and Atlantic (see 'Analysis'), the simulated open ocean inflow to the shelves strengthens by +11% (+2.5 Sv) and its mean NO_3 concentration increases by 0.6 mmol N m^{-3} during the twentieth century. The intensified circulation and enhanced productivity (+19%, Supplementary Fig. 2) cause an increase in OC export to the open ocean by 15% (+25.6 TgC yr^{-1}) and a downward change in Δp_{CO_2} by 31 ppm, increasing the coastal CO_2 uptake by 9.1 TgC yr^{-1}.

In the coastal ocean of high latitudes, expanding ice-free areas (springtime Arctic +25%, Antarctic +74%, Extended Data Fig. 4) strengthens the net CO_2 uptake by 3.3 gC m^{-2} yr^{-1} on the Arctic shelves and 10.1 gC m^{-2} yr^{-1} in the Antarctic coastal areas. Larger and longer-lasting open water areas give rise to both enhanced solubility and biological pumping (spring NPP Arctic +13%, Antarctic +33%), with a correlation between spring bloom productivity and sea ice cover of $r = -0.90$ ($P < 0.01$). Changes in the Arctic are alleviated by above-average warming by up to 1.4 °C (p_{CO_2} +9 ppm), which also compensates the effect of enhanced dilution (salinity −0.2 psu, p_{CO_2} −2 ppm) due to meltwater invasion from land (run-off +20%) and sea ice. The temperature effect decreases Δp_{CO_2} regionally (Fig. 2), but overall, the coastal CO_2 uptake is clearly enhanced (Fig. 4). Because of the different area covers, the total contribution of the Arctic shelves integrates to an increase in CO_2 absorption by 21 TgC yr^{-1}, which is much larger than for the comparatively narrow Antarctic shelves (8 TgC yr^{-1}).

To investigate the impact of the rising atmospheric p_{CO_2}, we continued experiments hist and woriv with atmospheric p_{CO_2} held constant (hist$_{ext}$ and woriv$_{ext}$). This allows us to differentiate the total F_{CO_2} signal into the solubility pump, driven by the dissolution of atmospheric CO_2 in the ocean, and the biological pump, driven by DIC assimilation due to phytoplankton growth (see 'Analysis' section), and quantify the import and export fluxes of the coastal carbon budget (Extended Data Table 1) sustaining these F_{CO_2} contributions (Fig. 5). Further discussion on the response of the ocean CO_2 sink to this idealized climate neutrality scenario is provided in section 'The response of the coastal ocean CO_2 uptake to climate neutrality'.

In the simulation without increasing nutrient input from rivers (woriv), the contribution to the CO_2 uptake signal by the solubility pump (−2.0 gC m^{-2} yr^{-1}; Fig. 5a) is larger than the contribution by the biological pump (−1.8 gC m^{-2} yr^{-1}; Fig. 5b). The additional CO_2 removed from the atmosphere either increases the coastal DIC inventory (55%) or is advected off-shelf (45%), thus weakening the net DIC flux from the open ocean (Fig. 5a, positive change in IC advective). The higher biological productivity due to enhanced upwelling and sea ice retreat (NPP +3.5%) results in higher advective export of OC but also respiratory CO_2, further reducing the net consumption of open ocean DIC by a similar amount (Fig. 5b, positive change in IC advective).

The enhanced nutrient supply from rivers (hist) strongly promotes phytoplankton growth in the coastal ocean (NPP +11%). The higher biological carbon fixation increases the biological contribution to the coastal CO_2 sink (to −2.8 gC m^{-2} yr^{-1}; Fig. 5d) and transforms this CO_2 into organic matter (Fig. 5c, OC advective). The river-induced boost in biological productivity increases the OC export (to the open ocean and sediments), the advective IC import (Fig. 5d, negative change in IC advective) and the CO_2 uptake from the atmosphere, and still leads to less DIC accumulation (IC stock) in coastal waters (all compared to woriv, $P < 0.01$). The increasing net import of IC from the open ocean (Extended Data Table 1, negative mean and negative change in IC advective) indicates that the coastal ocean might act to weaken the general DIC increase in the open ocean, since more open ocean DIC is consumed by biological productivity than respiratory CO_2 and riverine DIC loads are transported off-shelf. At the end of the twentieth century, this net

https://doi.org/10.1038/s41558-024-01956-w

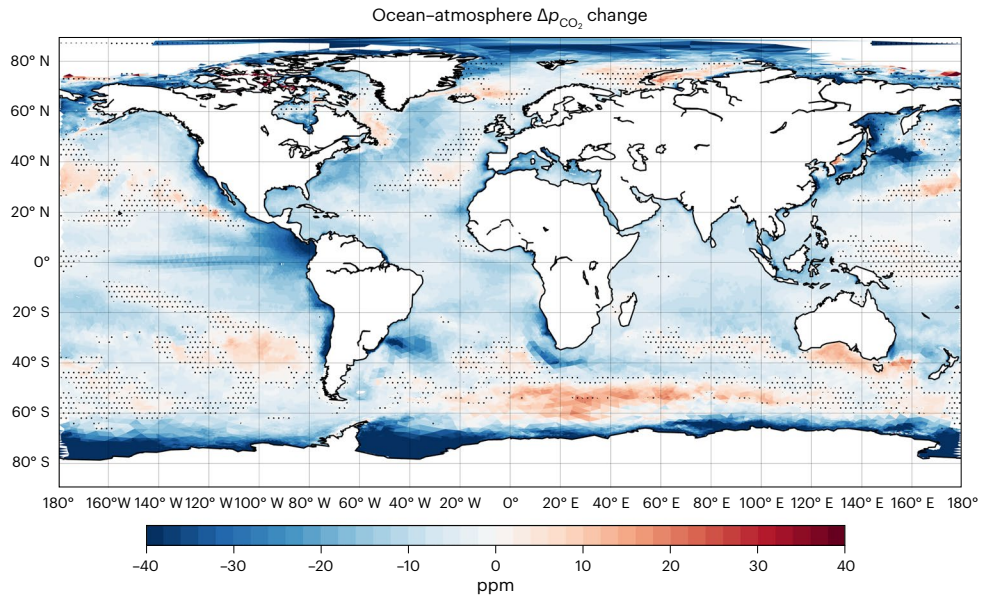

Fig. 2 | Simulated change signal of ocean–atmosphere Δp_{CO_2} during the twentieth century (1991–2010 of hist minus ctrl). Negative (blue) changes indicate that Δp_{CO_2} changed in a downward direction, that is, towards more uptake and less outgassing. White masked areas in the Arctic represent permanent sea ice cover, suppressing gas exchange at the sea surface. Dotted areas indicate changes with less than 95% confidence based on a 2-sided *t*-test.

DIC import from the open ocean is 125 TgC yr^{-1}, of which 82 TgC yr^{-1} are attributed to the impact of enhanced nutrient inputs from land (Fig. 3). When we subtract the DIC source of 85 TgC yr^{-1} due to simulated open ocean mineralization of terrestrial DOC, the coastal ocean is a weak net DIC sink of 40 TgC yr^{-1} for the open ocean. Thus, under the influence of increasing eutrophication, the coastal ocean is not only a growing sink for atmospheric CO_2, but also for upper ocean DIC, enhancing CO_2 uptake in the open ocean.

When increasing eutrophication is taken into account (hist), the biological contribution (−2.8 gC m^{-2} yr^{-1}) clearly exceeds the solubility contribution (−2.0 gC m^{-2} yr^{-1}), making biological carbon fixation the predominant process that intensifies the coastal CO_2 absorption during the twentieth century. This change is mediated by an enhanced export of OC to the open ocean, which is excluded from the gas exchange with the atmosphere, thus further adding to the carbon enrichment of the open ocean.

We can now quantify the main controls of the contemporary increasing CO_2 uptake in the coastal ocean (see 'Analysis' section). The solubility contribution is represented by the drop in the CO_2 uptake from hist to $hist_{ext}$ (Fig. 1) and accounts for 41% of the total F_{CO_2} signal during the twentieth century. The remaining 59% represents the biological contribution, which can be further attributed to a climate-induced component of 36% primarily driven by enhanced upwelling and sea ice retreat, and a river load-induced component of 23% represented by the difference between hist and woriv. This partitioning, however, includes the influence of changes in sea surface temperature and wind speed on F_{CO_2} (ref. 27), as well as the effect of the reduced CO_2 buffer capacity of sea water due to ocean acidification[28]. Lower CO_2 solubility and higher piston velocity due to increased water temperature both change by less than 1% and thus fairly cancel in their impact on F_{CO_2}. Generally higher wind speeds (by about 0.3 m s^{-1}), however, lead to stronger CO_2 exchange fluxes (by 10%), equally intensifying the solubility and biological carbon pumps. Moreover, simulated mean surface DIC concentration in the coastal ocean increases during the twentieth century by 29 mmol C m^{-3}, resulting in an increase of the Revelle factor from 10.1 to 10.7 (see 'Analysis'). This means that the p_{CO_2} gets more sensitive to changes in DIC and as a consequence, changes in carbon fixation and export processes have a higher impact on the p_{CO_2} and CO_2 gas exchange.

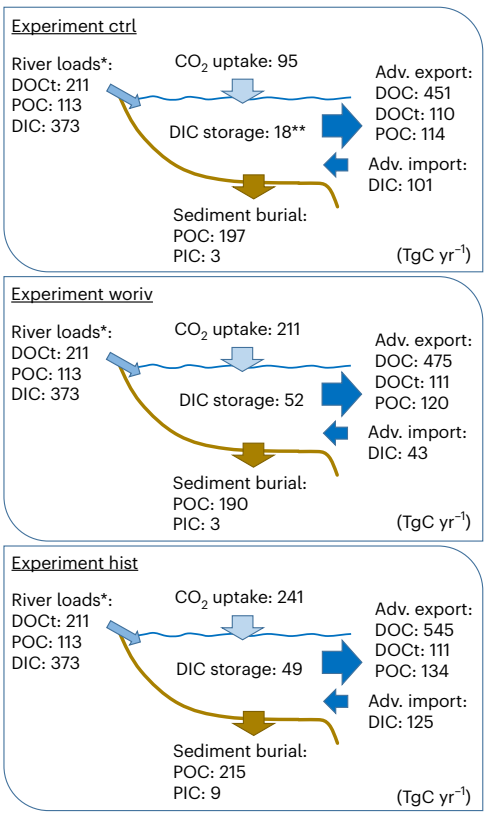

Fig. 3 | Carbon budget of the global coastal ocean, derived from experiments ctrl, woriv and hist for the period 1991–2010. All numbers are given in TgC yr^{-1}. *, riverine C inputs are prescribed and assumed to be constant over the simulation period. **, net DIC accumulation in the control run is due to long-term model drift. DOCt, terrestrial dissolved organic carbon; PIC, particulate inorganic carbon.

When we repeat the hist simulation without the historical rise in atmospheric p_{CO_2} (Extended Data Fig. 5), we find that the increase in coastal ocean CO_2 uptake is weaker by as much as 3.7 gC m^{-2} yr^{-1}

https://doi.org/10.1038/s41558-024-01956-w

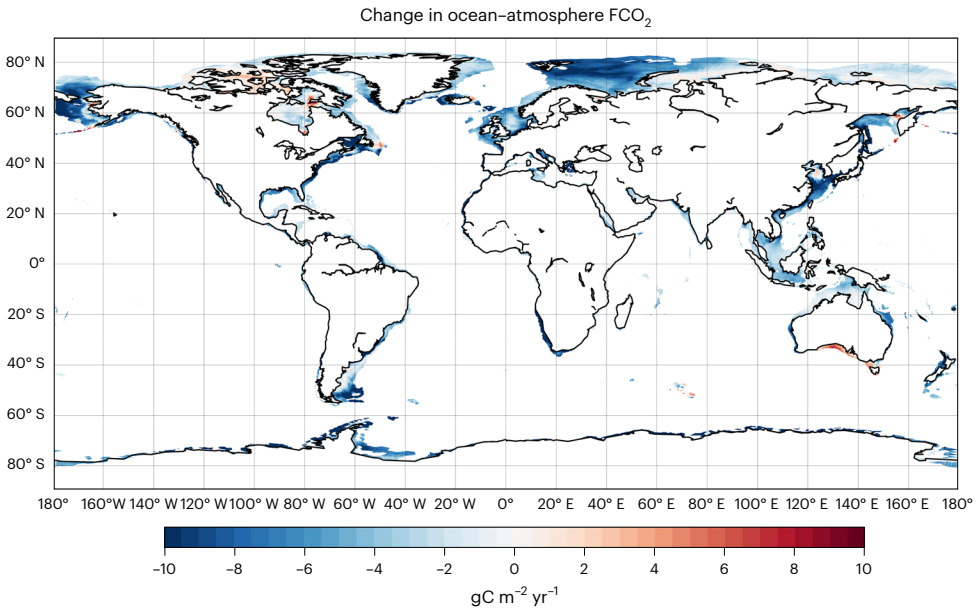

Fig. 4 | Simulated change signal of ocean–atmosphere CO_2 flux during the twentieth century (1991–2010 of hist minus ctrl), shown for the coastal ocean. Negative values indicate changes towards more CO_2 uptake and less outgassing.

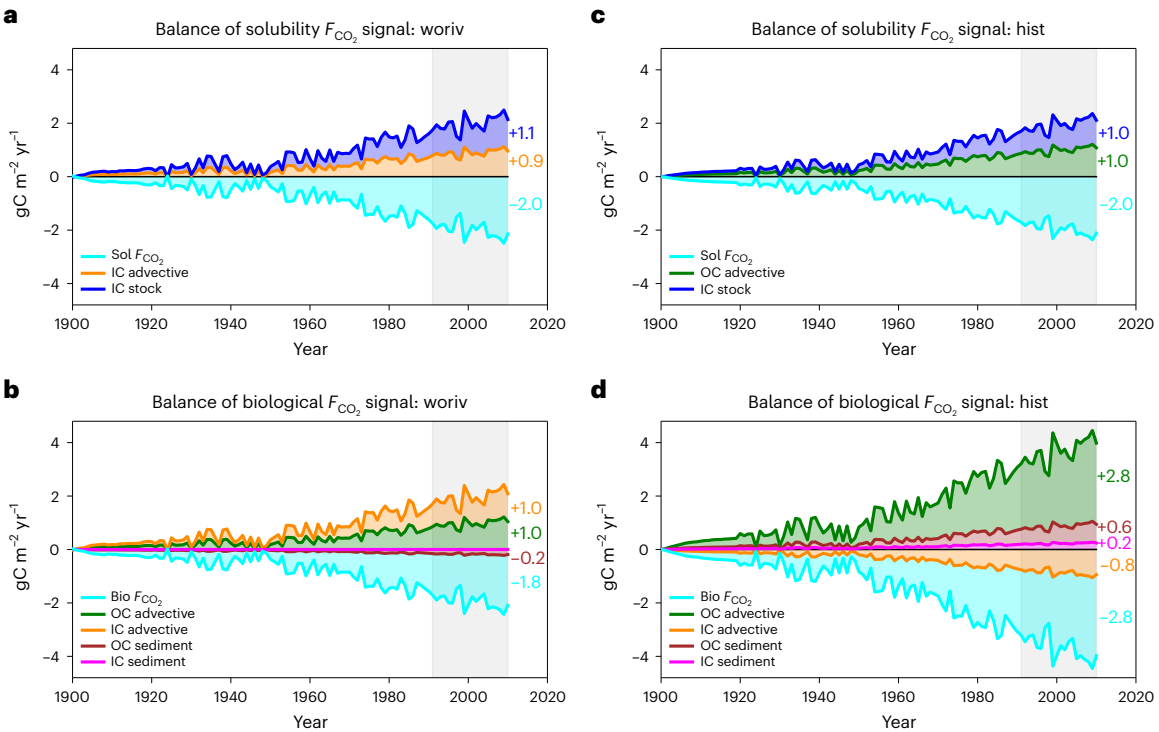

Fig. 5 | Partitioning of the coastal ocean F_{CO_2} signal into changes in the solubility and biological carbon pumps. a–d, Solubility (**a**,**c**) and biological contributions (**b**,**d**) for experiment woriv (**a**,**b**) (excluding increases in nutrient inputs from land) and the hindcast simulation hist (**c**,**d**). The sum of the solubility and biological contributions (cyan) corresponds to the total F_{CO_2} anomaly relative to ctrl. The solubility and biological signals as well as their sustaining net import and export fluxes are derived from the carbon budget of 1991–2010 (grey shaded area and values in the right figure margins) by assuming constant relative contributions over the whole simulation period. Negative changes in F_{CO_2} indicate increasing CO_2 uptake. OC/IC advective, net advective transport of organic/inorganic carbon to the open ocean; OC/IC sediment, net deposition of organic/inorganic carbon in shelf sediments; sol/bio F_{CO_2}, net solubility/biological CO_2 flux at the sea surface; IC stock, storage of inorganic carbon in shelf waters.

(1.1 instead of 4.8 gC m^{-2} yr^{-1}, $P < 0.01$), whereas the biological carbon fixation rate remains the same. This means that the biological contribution of the F_{CO_2} signal (2.8 gC m^{-2} yr^{-1}) is 60% driven by the buffer effect (1–1.1/2.8), as DIC assimilation by phytoplankton growth results in a larger p_{CO_2} decline when the CO_2 buffer capacity is low. This acidification impact has been shown to considerably enhance the biologically induced air–sea CO_2 gradient[29] and is here generalized to include the ocean margins. In the open ocean, without the buffer effect (Extended

Data Fig. 5), the warming impact on the CO_2 solubility would even outweigh the enhanced biological carbon sequestration, leading to a net reduction in CO_2 uptake by 0.4 gC m^{-2} yr^{-1}. Similarly, in the coastal ocean we identified the buffer effect as being the dominating control (60%) of the biological F_{CO_2} signal. The biological carbon fixation thus contributes substantially more to the CO_2 uptake as the buffer capacity decreases under continuous climate change.

During the twentieth century, changes in the CO_2 surface flux towards more uptake or less outgassing are represented in 93% of the coastal ocean area (Fig. 4). This general trend is visible in all latitudes, while impacts of the eutrophication signal are mainly restricted to the northern hemisphere (Extended Data Fig. 6, difference between woriv and hist) owing to the asymmetries in the spatial distribution of land masses, river run-off and associated nutrient inputs[30].

Contrasting the CO_2 uptake of the open ocean

According to our simulations, global oceanic NPP (Extended Data Fig. 7) increased through the twentieth century from 44.6 to 46.7 PgC yr^{-1} (+4.7%, $P < 0.01$), with an areal contribution of +4.3 gC m^{-2} yr^{-1} (+3.5%, $P < 0.01$) in the open ocean and a 5-times stronger signal of +21.0 gC m^{-2} yr^{-1} (+14.4%, $P < 0.01$) in the coastal ocean due to the impacts of enhanced upwelling, sea ice retreat and eutrophication (see 'Global increase in coastal net primary production'). While we have shown that this biological response substantially impacts the CO_2 absorption on the shelves, the resulting change in open ocean vertical POC export (+0.2 gC m^{-2} yr^{-1}, $P < 0.01$) contributes only 5% to the enhanced net CO_2 uptake (+4.0 gC m^{-2} yr^{-1}). This minor biological contribution is consistent with the estimate provided in ref. 31, which analysed apparent oxygen utilization as a proxy for biological productivity and concluded that 96% of the strengthening of the open ocean CO_2 sink during the recent decades was rather driven by physical and chemical processes. From the F_{CO_2} decline in experiment $hist_{ext}$, we obtain a chemically driven component of 71% (2.8 gC m^{-2} yr^{-1}), leaving 24% (1.0 gC m^{-2} yr^{-1}) as the remaining physical circulation-driven contribution of the F_{CO_2} signal in the open ocean.

Our next-generation model ICON-Coast reveals that the coastal ocean is a more efficient CO_2 sink than the open ocean (Fig. 1), being the first model to show agreement with this conclusion first deduced from observational products[3,7]. We find the largest differences in coastal versus open ocean CO_2 flux densities in low latitudes between ~30° S and 30° N. In these regions, biological carbon fixation leads to less coastal CO_2 outgassing and more uptake by 2.7 and 4.3 gC m^{-2} yr^{-1}, respectively, whereas in middle and high latitudes, coastal CO_2 flux densities do not exceed open ocean values. The divergent CO_2 exchange rates in low latitudes are well supported for the equatorial band of 10° S–10° N by the observational study of ref. 3, whereas for the remaining parts, this is less clear, albeit consistent with their uncertainty range.

The contrast between the coastal and open ocean CO_2 flux densities is strengthened by the dominance of subpolar and polar CO_2 sinks in the area distribution of the global coastal ocean[3]. The higher uptake efficiency of the coastal ocean, however, would also be maintained if the latitudinal area fraction was equally distributed, as the resulting net CO_2 uptake of 6.4 gC m^{-2} yr^{-1} in the coastal ocean would still exceed the 5.8 gC m^{-2} yr^{-1} of the open ocean. This suggests that another key factor controlling the disproportional CO_2 sink of the coastal ocean is high biological carbon fixation in low latitudes.

Our model shows the coastal ocean as a hotspot of carbon transformation processes, resulting in a biological CO_2 sink over the twentieth century. While such an autotrophic ocean has been put forward in previous model-based studies[11,22], changes in vertical and lateral carbon exchange fluxes are generally stronger by factors of 2–6 in our coast-specific model. That these fluxes are larger than previously assumed has implications for the missing link of the coastal ocean CO_2 flux in the global carbon budget[32], the source of OC for the open ocean[4], as well as biological impacts related to increased OC formation[33]. The dense carbon fluxes of the coastal ocean will probably face accelerating rates with forthcoming compound fossil emissions, climate change and human perturbations of freshwater systems. Our study thus provides a vital step for the assessment of historical and prospective evolutions of the coastal carbon cycle.

Online content

Any methods, additional references, Nature Portfolio reporting summaries, source data, extended data, supplementary information, acknowledgements, peer review information; details of author contributions and competing interests; and statements of data and code availability are available at https://doi.org/10.1038/s41558-024-01956-w.

References

1. Liu, K. K., Atkinson, L., Quiñones, R. & Talaue-McManus, L. in *Carbon and Nutrient Fluxes in Continental Margins: A Global Synthesis* (eds Liu, K. K. et al.) 3–24 (Springer, 2010).
2. Bauer, J. E. et al. The changing carbon cycle of the coastal ocean. *Nature* **504**, 61–70 (2013).
3. Roobaert, A. et al. The spatiotemporal dynamics of the sources and sinks of CO_2 in the global coastal ocean. *Global Biogeochem. Cycles* **33**, 1693–1714 (2019).
4. Regnier, P., Resplandy, L., Najjar, R. G. & Ciais, P. The land-to-ocean loops of the global carbon cycle. *Nature* **603**, 401–410 (2022).
5. Laruelle, G. G., Lauerwald, R., Pfeil, B. & Regnier, P. Regionalized global budget of the CO_2 exchange at the air–water interface in continental shelf seas. *Global Biogeochem. Cycles* **28**, 1199–1214 (2014).
6. Dai, M. et al. Carbon fluxes in the coastal ocean: synthesis, boundary processes, and future trends. *Annu. Rev. Earth Planet. Sci.* **50**, 593–626 (2022).
7. Laruelle, G. G. et al. Continental shelves as a variable but increasing global sink for atmospheric carbon dioxide. *Nat. Commun.* **9**, 454 (2018).
8. Hauck, J. et al. Consistency and challenges in the ocean carbon sink estimate for the global carbon budget. *Front. Mar. Sci.* **7**, 22 (2020).
9. Brewin, R. J. W. et al. Ocean carbon from space: current status and priorities for the next decade. *Earth Sci. Rev.* **240**, 104386 (2023).
10. Bourgeois, T. et al. Coastal-ocean uptake of anthropogenic carbon. *Biogeosciences* **13**, 4167–4185 (2016).
11. Lacroix, F., Ilyina, T., Mathis, M., Laruelle, G. G. & Regnier, P. Historical increases in land-derived nutrient inputs may alleviate effects of a changing physical climate on the oceanic carbon cycle. *Global Change Biol.* **27**, 5491–5513 (2021).
12. Mathis, M., Elizalde, A. & Mikolajewicz, U. The future regime of Atlantic nutrient supply to the Northwest European Shelf. *J. Mar. Syst.* **189**, 98–115 (2019).
13. Takahashi, T. et al. Global sea–air CO_2 flux based on climatological surface ocean pCO_2, and seasonal biological and temperature effects. *Deep Sea Res. II* **49**, 1601–1622 (2002).
14. Sundquist, E. T., Plummer, L. N. & Wigley, T. M. L. Carbon dioxide in the ocean surface: the homogeneous buffer factor. *Science* **204**, 1203–1205 (1979).
15. Takahashi, T. et al. Climatological mean and decadal change in surface ocean pCO_2, and net sea–air CO_2 flux over the global oceans. *Deep Sea Res. II* **56**, 554–577 (2009).
16. McKinley, G. et al. Timescales for detection of trends in the ocean carbon sink. *Nature* **530**, 469–472 (2016).
17. Wang, H., Hu, X., Cai, W. J. & Sterba-Boatwright, B. Decadal fCO_2 trends in global ocean margins and adjacent boundary current-influenced areas. *Geophys. Res. Lett.* **44**, 8962–8970 (2017).
18. Ward, N. D. et al. Representing the function and sensitivity of coastal interfaces in Earth system models. *Nat. Commun.* **11**, 2458 (2020).

19. Roobaert, A., Resplandy, L., Laruelle, G. G., Liao, E. & Regnier, P. A framework to evaluate and elucidate the driving mechanisms of coastal sea surface pCO_2 seasonality using an ocean general circulation model (MOM6-COBALT). *Ocean Sci.* **18**, 67–88 (2022).
20. Mathis, M. et al. Seamless integration of the coastal ocean in global marine carbon cycle modeling. *J. Adv. Model. Earth Syst.* **14**, e2021MS002789 (2022).
21. Bakker, D. C. E. et al. A multi-decade record of high-quality fCO_2 data in version 3 of the Surface Ocean CO_2 Atlas (SOCAT). *Earth Syst. Sci. Data* **8**, 383–413 (2016).
22. Lacroix, F., Ilyina, T., Laruelle, G. G. & Regnier, P. Reconstructing the preindustrial coastal carbon cycle through a global ocean circulation model: was the global continental shelf already both autotrophic and a CO_2 sink? *Global Biogeochem. Cycles* **35**, e2020GB006603 (2021).
23. DeVries, T. & Weber, T. The export and fate of organic matter in the ocean: new constraints from combining satellite and oceanographic tracer observations. *Global Biogeochem. Cycles* **31**, 535–555 (2017).
24. Daloz, A. S. & Camargo, S. J. Is the poleward migration of tropical cyclone maximum intensity associated with a poleward migration of tropical cyclone genesis? *Clim. Dyn.* **50**, 705–715 (2018).
25. Yang, H. et al. Poleward shift of the major ocean gyres detected in a warming climate. *Geophys. Res. Lett.* **47**, e2019GL085868 (2020).
26. Yang, H. et al. Tropical expansion driven by poleward advancing midlatitude meridional temperature gradients. *J. Geophys. Res. Atmos.* **125**, e2020JD033158 (2020).
27. Wanninkhof, R. Relationship between wind speed and gas exchange over the ocean revisited. *Limnol. Oceanogr. Methods* **12**, 351–362 (2014).
28. Sarmiento, J. L. & Gruber, N. *Ocean Biogeochemical Dynamics* (Princeton Univ. Press, 2006) .
29. Hauck, J. & Völker, C. Rising atmospheric CO_2 leads to large impact of biology on Southern Ocean CO_2 uptake via changes of the Revelle factor. *Geophys. Res. Lett.* **42**, 1459–1464 (2015).
30. Lacroix, F., Ilyina, T. & Hartmann, J. Oceanic CO_2 outgassing and biological production hotspots induced by pre-industrial river loads of nutrients and carbon in a global modeling approach. *Biogeosciences* **17**, 55–88 (2020).
31. Koeve, W., Kähler, P. & Oschlies, A. Does export production measure transient changes of the biological carbon pump's feedback to the atmosphere under global warming? *Geophys. Res. Lett.* **47**, e2020GL089928 (2020).
32. Friedlingstein, P. et al. Global carbon budget 2020. *Earth Syst. Sci. Data* **12**, 3269–3340 (2020).
33. Breitburg, D. et al. Declining oxygen in the global ocean and coastal waters. *Science* **359**, eaam7240 (2018).

Methods

Model description

The ocean-biogeochemistry model ICON-Coast is an advancement of the ocean component ICON-O[34,35] of the Hamburg Earth system model ICON-ESM[36]. Its adaptation to integrate coastal circulation features and carbon dynamics consists of a two-step development. First, a refinement of the horizontal grid resolution was confined to the continental margins and shallow shelves, including the transition zone to the adjacent deep ocean basins[20,37]. Second, the biogeochemistry component HAMOCC[38–40] was extended to better account for shelf-specific carbon transformation processes[20], including tidal currents and bottom drag effects[37], sediment resuspension[12], temperature-dependent remineralization in the water column[41] and sediment[20], variable sinking speeds of aggregated particulate carbon and mineral components[41], and matter fluxes from land, including river loads of terrestrial carbon and nutrients[11,30] as well as atmospheric deposition of dust[42] and nitrogen[40].

The dynamics of the model is based on the hydrostatic Boussinesq equations, which are solved on a triangular grid with Arakawa C-type staggering. In the configuration presented here, we used a biharmonic subgrid scale velocity closure with a scale-dependent viscosity coefficient to account for the variable horizontal resolution. Vertical mixing was parameterized by a prognostic equation for turbulent kinetic energy. Sea-ice dynamics were simulated by the sea-ice model FESIM[43]. Biogeochemical tracers in the water column were transported by the physical advection and diffusion schemes. Biological activity followed an extended nutrient, phytoplankton, zooplankton and detritus (NPZD) approach with a fixed stoichiometry and nutrient co-limitation of phosphate, nitrate, silicate and iron. Export production was separated into $CaCO_3$ and opal shell material. Sedimentary processes were represented by 12 biologically active layers, accounting for degradation and burial of organic and inorganic particulate matter, including pore water diffusion.

For our simulations here, we applied the same grid configuration used for the biogeochemistry runs in the model introduction paper[20]. The horizontal mesh spacing ranged from 160 km in the open ocean to 20 km near the coasts and along topographic gradients. The vertical was represented by 40 levels on z-coordinates, with a layer thickness of 10 m in the upper 100 m of the water column (except for the 16 m top layer with free surface elevation to facilitate tidal amplitudes and sea-ice draft) and increasing spacing below. The model time step in the presented setup was 720 s.

Experiment design

Our ocean simulations with ICON-Coast were driven with a number of prescribed boundary conditions. As atmospheric forcing fields, we used 3-hourly ERA-20C reanalysis data[44,45]. Annual mean atmospheric p_{CO_2} followed the historical record or the high-emissions global warming scenario RCP8.5, both as developed for the fifth IPCC Assessment Report (AR5). River run-off from ~2,000 catchment areas was reconstructed by the global hydrological discharge model HD[46]. Matter fluxes of DIP, DIN, DSi, DFe, DIC, Alkalinity, particulate organic matter and terrestrial dissolved organic matter were derived in refs. 11,30 for about the largest 850 rivers. Historically increasing nutrient loads of DIN and DIP were approximated by a linear increase during the hindcast period 1900–2010 (Supplementary Fig. 3). Atmospheric deposition of nitrogen and aeolian dust as further sources of inorganic nutrients followed refs. 40,42, respectively. Here, only 20% of the N deposition occurred in the coastal ocean, whereas 99% of the river inputs were discharged on the shelves (Supplementary Fig. 3). Aggregated over the coastal ocean area, the resulting total nutrient load from land thus primarily consisted of river inputs. In our analysis and discussion of the coastal ocean, we therefore mainly refer to the nutrient fluxes from land as river loads.

We initialized our spin-up procedure with an ocean state of the year 1900 from a historical simulation of the Earth system model MPI-ESM-HR as it contributed to the sixth Coupled Model Intercomparison Project (CMIP6). ICON-Coast was then run in physics-only mode for 200 years using looped forcing conditions of the period 1900–1919 to allow the ocean circulation to adjust to the model specifications and grid configuration. The biogeochemistry component was then included for another 100 years. The end of this spin-up run was used to initialize our production runs with transient forcing, as well as the control run as the continuation of the spinup with looped forcing.

The core simulation of this study is a hindcast run (hist) over the historical period 1900–2010, driven with the forcing conditions described in Table 1. To investigate the impacts of nutrient loads from rivers and the induced eutrophication signal in the coastal ocean, we contrasted this simulation with an experiment where the increase in nutrient inputs from land is excluded (woriv).

To further disentangle change signals in the CO_2 surface flux with respect to contributions from an active downward CO_2 pumping by the atmosphere or a passive CO_2 uptake flux that balances biological carbon sequestration, these simulations were extended for another 100 years by keeping the p_{CO_2} in the atmosphere at a constant level (Extended Data Fig. 2) and otherwise using looped forcing conditions over 1991–2010 ($hist_{ext}$ and $woriv_{ext}$). In these experiments, we ran the model into quasi-equilibrium of the upper ocean, indicated by a leveling of the CO_2 surface flux (Fig. 1). This additionally allowed us to estimate the response of the ocean CO_2 sink if we were to achieve global climate neutrality, or in our case if we had established climate neutrality since the year 2010. To contrast this response, we also set up an analogous counter experiment with continuously increasing CO_2 following emission scenario RCP8.5 ($woriv_{inc}$).

Increasing CO_2 uptake by the ocean is associated with a decrease in the ability of the sea water to further absorb any additional CO_2, which means that changes in DIC concentrations would induce stronger changes in p_{CO_2} and hence in CO_2 gas exchange. To quantify the impact of this buffer effect on the biological CO_2 uptake, we conducted experiment $woco_2$, which is the same as the hindcast hist but keeping atmospheric p_{CO_2} at the level of the year 1900 (as for the control run ctrl). As we have not analysed this experiment further, it is only shown in Extended Data Fig. 5.

Model evaluation

To evaluate our model results, we compared the last 10 years (2001–2010) of the hindcast simulation hist with best estimates from observation-based upscalings. Global fields of NPP and surface CO_2 flux are shown in Supplementary Fig. 4, with a simulated total productivity of 48 GtC yr^{-1} and a net CO_2 uptake of 2.2 GtC yr^{-1}. These global values are consistent with the contemporary observational ranges of 39–58 GtC yr^{-1} for NPP[47–49] and 2.0–2.6 GtC yr^{-1} for CO_2 absorption during the period 1994–2007[50,51]. Biases in surface nutrients (nitrate −2.47 mmol m^{-3} and phosphate −0.13 mmol m^{-3}) compared with the World Ocean Atlas 2013[52] are mainly found in the Southern Ocean (Supplementary Fig. 4c), probably related to underestimated iron limitation in the biological nutrient consumption.

Simulated surface p_{CO_2} shows a qualitative distribution consistent with the reconstruction in ref. 53 based on SOCAT data of the period 1998–2015 (Supplementary Fig. 5), but values are generally overestimated with a mean bias of +16 ppm in the coastal ocean and +11 ppm in the open ocean. To get the local mean Δp_{CO_2} in agreement with observations, we applied a linear bias correction of simulated p_{CO_2} against ref. 53 by subtracting the climatological differences of the period 2001–2010 at every grid cell. This resulted in an offset of the simulated p_{CO_2} time series, while the simulated seasonality or the long-term trend of the time series remained unaffected. CO_2 fluxes at the sea surface, however, were not adjusted to ensure a closed mass balance. The anthropogenic signal of the global ocean CO_2 uptake (Supplementary Fig. 6) thus seemed to be slightly weaker compared with best estimates by the Global Carbon Budget[32], but still lay within the range of uncertainty.

Net primary production was particularly well captured in the coastal ocean (Extended Data Fig. 1), best demonstrating the added value of ICON-Coast compared with conventional global models that are designed for open ocean biogeochemistry. Our simulated coastal carbon budget for the period 2001–2010 was characterized by a lateral carbon export from continental shelf waters to the open ocean of 0.79 GtC yr^{-1}, which is comparable to the observation-based range of 0.85–0.95 GtC yr^{-1} (refs. 2,4). Carbon burial in the shelf sediments was simulated to be 0.22 GtC yr^{-1} and DIC accumulation in the water column to be 0.03 GtC yr^{-1}, which in total was estimated to be 0.30 ± 0.11 GtC yr^{-1} in ref. 4. The carbon export fluxes induced a simulated net CO_2 uptake of 0.25 GtC yr^{-1} from the atmosphere, in good agreement with observational estimates of 0.19–0.30 GtC yr^{-1}[2–6].

Further evaluation of the model performance in representing coastal carbon dynamics can be found in ref. 20. The model parameters and grid configuration we use here are identical to the setup in ref. 20 used for the simulation including ocean biogeochemistry. The differences are therefore only in the prescribed external forcing, as our simulations cover the entire twentieth century rather than just the evaluation period 2000–2010. We used ERA-20C reanalysis for the meteorological forcing instead of ERA-Interim, and we used transient atmospheric p_{CO_2} as well as riverine nutrient loads, which were held constant in ref. 20.

Due to limitations in computational resources, the simulations presented here were initialized from a global ocean state that was not in internal model equilibrium. The remaining long-term drift after spinup is reflected by an ongoing adjustment of biogeochemical tracers at the sea surface, for example, of +0.015 mmol m^{-3} (100 yr)$^{-1}$ phosphate and +3.0 mmol m^{-3} (100 yr)$^{-1}$ silicate, leading to an increase in coastal DIC storage in the control run of 0.6 gC m^{-2} yr^{-1} (IC stock in Extended Data Table 1). To account for the model drift in our analysis, we determined change signals through the simulation period relative to the control run (see next section).

Analysis

Coastal regions often show strong spatial gradients in water mass characteristics between the shallow proximal zone and the outer shelf areas with water depths reaching 500 m along the continental margin. These deeper regions are less affected by tidal mixing and promote extensive vertical fluxes of carbon and nutrients out of the biologically productive surface layers, thus playing an integrative role in the functioning of the shelf carbon pump[54–57]. For our definition of the coastal ocean, we therefore used the area spanning from the coastline to the 500 m isobath to properly include the deeper shelves such as the Barents Sea, the Greenland Shelf or the outer part of the Patagonian Shelf[58].

The EBUS we are referring to comprise the California (20° N–43° N) and Humboldt (8° S–40° S) upwelling systems in the eastern Pacific, and the Canary (18° N–43° N) and Benguela (15° S–32° S) upwelling systems in the eastern Atlantic.

Anthropogenically forced signals during the simulation period 1900–2010 refer to changes that are induced by anthropogenic perturbations, here increasing atmospheric CO_2 and riverine nutrient loads. These changes were evaluated relative to the background of natural variability, which is idealized by the control experiment of stable 1900–1919 forcing conditions. Our results thus do not include alterations in the marine carbon budget during early industrialization between 1750 and 1900. Change signals through the twentieth century were calculated as means over the period 1991–2010 of a particular simulation minus the same period of the control ctrl run, thus removing contributions due to long-term model drift. Moreover, the change signals were tested at the 95% confidence level to account for influences of decadal variability. Further low-frequency variations in time series were evaluated by autocorrelation analysis. For the import and export fluxes of the coastal carbon budget (Extended Data Table 1), autocorrelation coefficients calculated for lags of 1–50 years were generally lower than ±0.2.

The Revelle factor is used to quantify the CO_2 buffer capacity of sea water. This is a measure of the amount of atmospheric CO_2 that can be taken up by the ocean. We calculated the Revelle factor as the ratio between fractional changes in ocean p_{CO_2} and DIC[28].

In our experiments, we considered three external perturbations that can alter the CO_2 exchange at the sea surface (see 'Experiment design'). The meteorological forcing (1) determines the physical climate that primarily affects the water temperature and stratification of the upper ocean, as well as the ocean circulation. Changes in this forcing therefore impact the CO_2 solubility of sea water and the lateral exchange fluxes of carbon between the continental shelves and the adjacent open ocean. The atmospheric p_{CO_2} (2) impacts the ocean–atmosphere p_{CO_2} gradient and therefore the thermodynamic force of the CO_2 flux. Nutrient inputs from land (3) fuel marine primary production and thus impact DIC concentrations and p_{CO_2} at the sea surface.

Our quantification of the main contributions to the increasing CO_2 uptake in the coastal ocean was based on the extended simulations with constant atmospheric p_{CO_2} and stable meteorological forcing ($hist_{ext}$ and $worivi_{ext}$). The equilibrium state of these experiments describes an end-of-twentieth-century carbon budget that has been deprived by the rapid increase in atmospheric p_{CO_2}, and the resulting drop in CO_2 uptake (Fig. 1) represents the solubility contribution to the historical F_{CO_2} signal caused by CO_2 pumping from the atmosphere. In $hist_{ext}$, this solubility contribution is 41% (−2.0 gC m^{-2} yr^{-1}) of the total F_{CO_2} signal (−4.8 gC m^{-2} yr^{-1}). The remaining contribution of 59% is driven in the reversed causal direction, that is, CO_2 being sucked up by the ocean due to biological carbon fixation, compensating uptake-weakening physical effects of global-scale warming, such as reduced CO_2 solubility or a shoaling and strengthening of the stratification (global mean changes in winter-time mixed-layer depth −23 m and stratification +10%). As we found that ocean-shelf volume transports did not significantly change, in the coastal ocean this non-chemical contribution to the historical F_{CO_2} signal (Fig. 1) is therefore dominated by biologically enhanced carbon fluxes, allowing us to commonly refer here to the biological contribution. Experiment $worivi_{ext}$ allowed us to further attribute the biological contribution to a climate-induced component of 36% and a river load-induced component of 23%. Furthermore, as the climate-induced changes were retained in the extended runs due to the stable meteorological forcing, the carbon fluxes related to biological productivity were also representative for their correlates at the end of the original experiments hist and worivi, differing by only 1 gC m^{-2} yr^{-1} in NPP and 0.03–0.06 gC m^{-2} yr^{-1} in the advective OC export to the open ocean and the vertical OC and IC exports to the sediment. In the extended runs, the advective IC flux thus closed the balance between all oceanic export fluxes (lateral and vertical) and the biologically driven CO_2 uptake from the atmosphere. Hence, by comparing the carbon budgets of the original and extended simulations, we can derive how the solubility and biological contributions to the change in the CO_2 surface flux are balanced by the import and export fluxes through the sediment and open ocean boundaries (Fig. 5).

When increasing nutrient inputs from land were excluded from the forcing (worivi), the F_{CO_2} change signal of −3.8 gC m^{-2} yr^{-1} (Extended Data Table 1) divided into a biological contribution of −1.8 gC m^{-2} yr^{-1} (the equilibrium F_{CO_2} in $worivi_{ext}$) and a slightly larger solubility contribution of −2.0 gC m^{-2} yr^{-1} due to atmospheric pumping (the F_{CO_2} drop from worivi to $worivi_{ext}$). Moreover, the coastal ocean contains more respiratory CO_2 (Fig. 5b), represented by a change in the advective IC flux of +1.0 gC m^{-2} yr^{-1} in experiment $worivi_{ext}$ (relative to ctrl). In the original worivi run, however, the advective IC flux changed by +1.9 gC m^{-2} yr^{-1} (Extended Data Table 1), which means that another 0.9 gC m^{-2} yr^{-1} of this weakening net IC import consists of additional CO_2 delivered by the atmosphere. As this term balanced all changes in

the export fluxes, the remaining 1.1 gC m^{-2} yr^{-1} of the total CO_2 provided by atmospheric pumping are accumulating in the water column, reflected by the increase in depth-integrated DIC (IC stock in Extended Data Table 1).

The additional nutrient supply from rivers strongly promoted phytoplankton growth in the coastal ocean (NPP +11%) and induced primary producers to utilize atmospheric CO_2 pumping as a carbon source. In the hindcast simulation hist, the F_{CO_2} change signal of −4.8 gC m^{-2} yr^{-1} contained a solubility contribution of −2.0 gC m^{-2} yr^{-1} but a larger biological contribution of −2.8 gC m^{-2} yr^{-1} due to eutrophication (Fig. 5c). The higher organic matter production also affected the carbon export rates, compared with woriv. In $hist_{ext}$, the change in the advective IC flux was −1.8 gC m^{-2} yr^{-1} (relative to ctrl), which represents the additional net DIC import from the open ocean that would be required to provide enough IC for the marked increase in organic matter production, if we had constant p_{CO_2} in the atmosphere (and hence no further chemical CO_2 pumping as a source of IC). The factual change in net open ocean IC import in hist, however, was only −0.8 gC m^{-2} yr^{-1} (IC advective in Extended Data Table 1). This discrepancy indicates that the enhanced biological production in hist also consumes 1.0 gC m^{-2} yr^{-1} (50%) of the additional CO_2 pumped in from the atmosphere. This potentially limits the biological impact on the total F_{CO_2} signal (relative to woriv); however, it eliminates a considerable source term of DIC for the open ocean. As this contribution again balanced all changes in the carbon export fluxes, the remaining 1.0 gC m^{-2} yr^{-1} of the atmospheric CO_2 pumping are accumulating in the water column (IC stock in Extended Data Table 1).

Model limitations and uncertainties

Our approach in global-scale coastal modelling opens the possibility to include more relevant processes that have not yet been taken into account in our simulations. We show that enhanced biological carbon fixation due to riverine nutrient inputs strengthens the CO_2 sink of the coastal ocean as well as the off-shelf transport of organic matter. In our river loadings, however, we neglected the still uncertain augmentation of OC transports to the ocean, which was estimated at ~5–10% since preindustrial times (ref. 4 and citations therein). DOC concentrations in the model were generally low, reaching 150 mmol C m^{-3} in highly productive coastal areas such as the East China Shelf, whereas measurements range between 100 and 300 mmol C m^{-3} (ref. 59). As terrestrial organic matter typically causes a CO_2 source following mineralization in the ocean, increased OC inputs from land could potentially weaken the net CO_2 uptake in the coastal ocean. In our approach, a 5–10% increase would correspond to an additional input of 16–32 TgC yr^{-1}. Taking into account that a fraction of ~40–60% is mineralized in the coastal ocean, as suggested in published literature[22] and confirmed here, the CO_2 uptake could be weakened by 6–19 TgC yr^{-1} by increasing OC inputs. We also assumed that the advective OC export to the open ocean would rise by a similar amount. Considering that the difference in CO_2 uptake between experiments hist and woriv is 30 TgC yr^{-1}, the river-induced increases in net CO_2 uptake would still override a potentially weaker CO_2 uptake caused by rising OC inputs.

The incorporation of other sources of land-derived matter loadings, however, would further constrain their quantitative impact on coastal CO_2 uptake and help estimate responses to future climate change. Groundwater discharge provides regionally eminent inputs of soluble carbon and nutrients to the coastal ocean of up to 25% of the river fluxes[60]. Carbon reservoirs in tidal flats and intertidal wetlands are shrinking due to sea level rise, resulting in net carbon fluxes to the ocean and atmosphere of ~5 TgC yr^{-1} (ref. 61). On the Arctic shelves, additional carbon and nutrient supply due to coastal erosion is ~60% higher than fluvial inputs[62,63] and is expected to further increase with global warming[64]. The CO_2 uptake in the northern high latitudes might thus become generally weaker when effects of coastal erosion are taken into account. Nevertheless, drivers of primary productivity and related carbon fluxes in a widely changing Arctic were shown to depend on various processes, events and features across different spatial and temporal scales[65]. Our model results for the Arctic may therefore be associated with comparatively high uncertainty.

According to our simulations, the coastal ocean is a more efficient CO_2 sink than the open ocean. The potentially overestimated flux densities in the Arctic coastal regions due to missing carbon inputs might be compensated by too high ocean p_{CO_2} in particular in the Canadian sector (Supplementary Fig. 5), which probably weakens the simulated net CO_2 absorption north of ~50° N. In the low latitudes, the divergent CO_2 exchange rates between the coastal and open ocean are well supported by the observational study of ref. 3.

Simulated oxygen concentrations on the shelves are generally higher than ~0.2 mmol O_2 m^{-3}, hence the model does not capture anoxic conditions in shallow coastal areas. In the current model configuration, the water column has to be represented in the model by at least two vertical layers. In the grid configuration used here, the minimum vertical resolution of 10 m comes with limitations in representing shallow stratification that would limit the ventilation of subsurface water masses, as well as the resupply of nutrients to the sea surface. Moreover, the model currently misses the impact of water turbidity on irradiance and light penetration depth as a control factor of coastal carbon dynamics. This is particularly relevant in areas where strong tidal currents induce sediment resuspension, as well as in regions with high river inputs of particulate matter.

The coarse vertical resolution may also limit the representation of low aragonite/calcite saturation states of coastal waters, including sediment pore water[66]. The simulated increase in particulate IC sedimentation is therefore probably overestimated. Nevertheless, the sedimentation rate of 0.09 PgC yr^{-1} in 1991–2010 is still comparatively low, as the model does not include contributions from coral reefs and seagrass-dominated embayments, which are estimated to account for 70–80% of the total carbonate burial of 0.16 PgC yr^{-1} in the coastal ocean (ref. 67).

In our simulations, enhanced upwelling in eastern boundary upwelling systems is associated with more CO_2 uptake, driven by increased biological carbon fixation that compensates for the impact of higher DIC concentrations of upwelled water masses on surface p_{CO_2}. From an observational point of view, however, the net effect of intensified upwelling on p_{CO_2} in eastern boundary regions is still unclear. The influence of cold water masses from intermediate depths could sustain global warming and even lead to lower sea surface temperature[68,69] and p_{CO_2} (ref. 13), while trend analyses of the California upwelling system over shorter time periods[17] rather suggest a p_{CO_2} increase in the ocean that exceeds the rate of change in the atmosphere.

The finest horizontal grid resolution of 20 km used in the simulations presented here is a considerable improvement in global modelling approaches on coastal ocean dynamics. Yet, a mesh spacing of 1–5 km is required to resolve the characteristic spatial scales on most shallow shelves[70]. Processes related to circulation features smaller than ~40–80 km are therefore still underrepresented in our results[71]. This potentially affects, for instance, the formation of tidal fronts and cross-frontal exchange[72], vertical mixing due to internal waves[73], and the transport of heat and biogeochemical tracers by small-scale and meso-scale eddies[74]. As high-resolution Earth system modelling is still in its infancy, it is unknown how these processes would modify the carbon fluxes in the global coastal ocean and interact with the larger-scale dynamics of the ocean and atmosphere.

Our results were derived from a single global ocean-biogeochemistry simulation. We are thus unable to evaluate the sensitivity of our findings to the specific parameter setup used here and to general model uncertainties. In view of the high heterogeneity in the dominating physical and biogeochemical controls on regional carbon dynamics, this constraint is of particular relevance as the calculation of the coastal carbon budget ensues from the balance of huge cross-shelf

volume transports in the order of 500 Sv (1 Sv = 10^6 m^3 s^{-1})[75]. These limitations underline the urgent need for further development on the representation of coastal carbon dynamics in global modelling approaches to better constrain uncertainties in our findings, which would help deepen a quantitative understanding of the role of the land–ocean transition zone in the global carbon cycle.

The response of the coastal ocean CO_2 uptake to climate neutrality

Our coastal carbon budget suggests that the DIC accumulation in the shelf waters during the past decades was a chemically driven process (IC stock in Fig. 5a,c). Accordingly, as atmospheric p_{CO_2} continued to increase in experiment $woriv_{inc}$, the CO_2 uptake of the ocean kept growing without discernible disruption (Fig. 1). In an idealized climate neutrality scenario with atmospheric p_{CO_2} and meteorological forcing fields held stable (experiments $woriv_{ext}$ and $hist_{ext}$), by contrast, the CO_2 uptake started to weaken dramatically with a short delay of ~3–4 years. The relaxation time needed for the upper ocean to chemically equilibrate with the atmosphere was ~100 years for both the coastal and open ocean. The progression, however, had an asymptotic shape, where half of the F_{CO_2} drop occurred in the first 1–2 decades. In the coastal ocean, the F_{CO_2} relaxation of $hist_{ext}$ followed experiment $woriv_{ext}$ with a remarkably stable offset of ~1.4 gC m^{-2} yr^{-1} (Supplementary Fig. 7), resulting from land-derived nutrient inputs. Thus, although these two experiments distinctly differed in their biological carbon fluxes, the biology had hardly any influence on the equilibration process. The net impact of biological carbon sequestration is neither speeding up equilibration due to an increased surface CO_2 flux, nor retarding equilibration by continuously removing CO_2 that has been absorbed from the atmosphere. This result is consistent with the finding that respiratory CO_2 does not accumulate on the shelves (IC advective in Fig. 5b), reinforcing chemical dominance also in the equilibration mechanism.

Similar to the response in the coastal ocean, the CO_2 uptake in the open ocean continued to increase with further increasing atmospheric p_{CO_2} ($woriv_{inc}$) but broke down drastically as soon as atmospheric p_{CO_2} levelled off (Fig. 1a), with a comparable equilibration time of ~100 years. In the open ocean, however, this time scale would be influenced by the depth of the mixed layer, the stability of the stratification and the intensity of vertical mixing. Since the range in the vertical structure of the water column as simulated by different global models is relatively high[76], we expect a similar model uncertainty in the CO_2 flux relaxation time. Using the UVic Earth System Model for example, ref. 77 obtained a comparable sudden drop in the global ocean CO_2 uptake after atmospheric CO_2 stopped rising, but a distinctly longer relaxation time of ~200–300 years for present-day climate conditions.

The biological fluxes, however, determine the equilibrium level of the CO_2 uptake, as the CO_2 exchange with the atmosphere dynamically balances the oceanic sources and sinks of inorganic carbon. In the coastal ocean, the higher biological productivity fuelled by increasing riverine nutrient inputs (experiments hist and $hist_{ext}$) led to a total increase in the biological contribution to F_{CO_2} of 2.8 g m^{-2} yr^{-1}. Because of the much higher biological change signal in the coastal ocean compared with the open ocean (see 'Contrasting the CO_2 uptake of the open ocean'), we found that the relative F_{CO_2} drop under constant atmospheric p_{CO_2} ($hist_{ext}$) was weaker in the coastal ocean by ~30% (Fig. 1) and the equilibrium F_{CO_2} was higher by a factor of 2 (coastal ocean 6.2 g m^{-2} yr^{-1}, open ocean 3.1 gC m^{-2} yr^{-1}). This means that in a climate neutrality scenario, the global ocean CO_2 sink weakens by 0.91 PgC yr^{-1} (Supplementary Table 1), but the coastal ocean gains relevance as its contribution to the total oceanic uptake increases from the currently 11% (end of hist) to 16%.

Note, however, that this scenario is not a consistent future projection, as we are missing the physical response of the coupled ocean–atmosphere climate system, as well as natural variations in atmospheric p_{CO_2}. Nevertheless, our simulated oceanic response to atmospheric p_{CO_2} levelling is consistent with previous global model simulations[77] and is here demonstrated to include the continental shelves, despite their generally more intense carbon transformation and exchange processes. Yet, a higher coastal CO_2 uptake is maintained by enhanced biological carbon fixation. Under an effective emissions reduction policy, the coastal ocean would thus remain a stronger CO_2 sink than the open ocean (per unit area), sustaining an increased ocean–shelf gradient in CO_2 flux density. This implies that the future CO_2 uptake of the coastal ocean is crucially influenced by the growth rates of atmospheric greenhouse gas concentrations and matter fluxes from land.

Global increase in coastal net primary production

Our model results suggest that biological carbon fixation provided an essential contribution to the increase in coastal ocean CO_2 uptake during the past century. To evaluate the simulated increase in coastal NPP, we here compared our model results with observational estimates derived from satellite products.

The simulated increase in mean coastal NPP is 21 gC m^{-2} yr^{-1}. This signal is mainly driven by increasing nutrient inputs from land (76%), enhanced upwelling in eastern boundary upwelling systems (10%) and growing open water areas in high latitudes due to sea ice retreat (4%). Riverine nutrient inputs directly fuel NPP in near-shore areas of large river systems[78], upwelling mixes nutrient-rich water masses from intermediate depths to the euphotic zone[79], and sea ice retreat leads to larger and longer-lasting open water areas, promoting NPP via more favourable light conditions[80].

The immediate impact of biological carbon fixation on ocean p_{CO_2} and air–sea gas exchange is dependent on the sea water capacity to hold CO_2 (ref. 28). This buffer capacity weakens with increasing DIC concentrations in the ocean in the course of rising CO_2 emissions to the atmosphere, leading to a higher sensitivity of sea water p_{CO_2} to DIC changes. In the global coastal ocean, we found that the buffer effect accounts for 60% of the increase in the biological carbon pump (see main part). Because sea water chemistry is further influenced by temperature, this impact is intensified towards the poles[81]. In high latitudes, the process of biological carbon fixation therefore translates into a p_{CO_2} drop that is larger than in low latitudes, resulting in a larger biological control of the ocean–atmosphere p_{CO_2} gradient and thus CO_2 exchange. On the broad Arctic shelves, the contribution of the buffer effect to the biological F_{CO_2} signal is even 75%.

We analysed the time series of 11 satellite products for NPP provided by the Ocean Productivity project (http://sites.science.oregonstate.edu/ocean.productivity/custom.php, accessed 18 December 2023). The data cover periods that range between 10 and 20 years only (MODIS 20 years, SeaWiFS 10 years, VIIRS 10 years), impeding an evaluation of long-term trends. Nevertheless, the majority of the calculated decadal trends show a consistent increase for the global coastal ocean, as well as for subareas of the eastern boundary upwelling systems and the Arctic shelves (Supplementary Table 2). Moreover, the increasing trends are generally larger for the coastal ocean than for the open ocean (by factors of 5–10), in line with our model results. The potentially too-low trend in Arctic productivity may indicate that the simulated impact of the biological carbon pump on the CO_2 uptake in high latitudes might be underestimated. For illustration, all time series have been standardized (Supplementary Fig. 8) to account for the high uncertainty in satellite-derived NPP[82].

Data availability

Primary model output used for creating the figures shown here is freely accessible on the Zenodo archive[83].

Code availability

The model code of ICON-Coast is available to individuals under licences (https://mpimet.mpg.de/en/science/modeling-with-icon/

code-availability). By downloading the ICON-Coast source code, the user accepts the licence agreement. The source code of ICON-Coast used in this study can be obtained from the Zenodo archive[84]. Climate Data Operators were used for analyses (https://code.mpimet.mpg.de/projects/cdo/). Figures including maps were made with Natural Earth and Cartopy (https://scitools.org.uk/cartopy).

References

34. Korn, P. Formulation of an unstructured grid model for global ocean dynamics. *J. Comput. Phys.* **339**, 525–552 (2017).
35. Korn, P. & Linardakis, L. A conservative discretization of the shallow-water equations on triangular grids. *J. Comput. Phys.* **375**, 871–900 (2018).
36. Jungclaus, J. H. et al. The ICON Earth System Model version 1.0. *J. Adv. Model. Earth Syst.* **14**, e2021MS002813 (2022).
37. Logemann, K., Linardakis, L., Korn, P. & Schrum, C. Global tide simulations with ICON-O: testing the model performance on highly irregular meshes. *Ocean Dyn.* **71**, 43–57 (2021).
38. Ilyina, T. et al. The global ocean biogeochemistry model HAMOCC: model architecture and performance as component of the MPI-Earth System Model in different CMIP5 experimental realizations. *J. Adv. Model. Earth Syst.* **5**, 287–315 (2013).
39. Paulsen, H., Ilyina, T., Six, K. D. & Stemmler, I. Incorporating a prognostic representation of marine nitrogen fixers into the global ocean biogeochemical model HAMOCC. *J. Adv. Model. Earth Syst.* **9**, 438–464 (2017).
40. Mauritsen, T. et al. Developments in the MPI-M Earth System Model version 1.2 (MPI-ESM1.2) and its response to increasing CO_2. *J. Adv. Model. Earth Syst.* **11**, 998–1038 (2019).
41. Maerz, J., Six, K. D., Stemmler, I., Ahmerkamp, S. & Ilyina, T. Microstructure and composition of marine aggregates as co-determinants for vertical particulate organic carbon transfer in the global ocean. *Biogeosciences* **17**, 1765–1803 (2020).
42. Mahowald, N. et al. Climate response and radiative forcing from mineral aerosols during the last glacial maximum, pre-industrial, current and doubled-carbon dioxide climates. *Geophys. Res. Lett.* **33**, L20705 (2006).
43. Danilov, S. et al. Finite-element sea ice model (FESIM), version 2. *Geosci. Model. Dev.* **8**, 1747–1761 (2015).
44. Poli, P. et al. *The Data Assimilation System and Initial Performance Evaluation of the ECMWF Pilot Reanalysis of the 20th-century Assimilating Surface Observations Only (ERA-20C)* ERA Report Series 14 (ECMWF, 2013).
45. Poli, P. et al. *ERA-20C Deterministic* ERA Report Series 20 (ECMWF, 2015).
46. Hagemann, S., Stacke, T. & Ho-Hagemann, H. T. M. High resolution discharge simulations over Europe and the Baltic Sea catchment. *Front. Earth Sci.* **8**, 12 (2020).
47. Buitenhuis, E. T., Hashioka, T. & Quéré, C. L. Combined constraints on global ocean primary production using observations and models. *Global Biogeochem. Cycles* **27**, 847–858 (2013).
48. Richardson, K. & Bendtsen, J. Vertical distribution of phytoplankton and primary production in relation to nutricline depth in the open ocean. *Mar. Ecol. Progr. Ser.* **620**, 33–46 (2019).
49. Kulk, G. et al. Primary production, an index of climate change in the ocean: satellite-based estimates over two decades. *Remote Sens.* **12**, 826 (2020).
50. Gruber, N. et al. The oceanic sink for anthropogenic CO_2 from 1994 to 2007. *Science* **363**, 1193–1199 (2019).
51. Watson, A. J. et al. Revised estimates of ocean–tmosphere CO_2 flux are consistent with ocean carbon inventory. *Nat. Commun.* **11**, 4422 (2020).
52. Garcia, H. E. et al. *World Ocean Atlas 2013, Volume 4, Dissolved Inorganic Nutrients (Phosphate, Nitrate, Silicate)* NOAA Atlas NESDIS 76 (NOAA, 2014).
53. Landschützer, P., Laruelle, G. G., Roobaert, A. & Regnier, P. A uniform pCO_2 climatology combining open and coastal oceans. *Earth Syst. Sci. Data* **12**, 2537–2553 (2020).
54. Holt, J. et al. Modelling the global coastal ocean. *Philos. Trans. A: Math Phys. Eng. Sci.* **367**, 939–951 (2009).
55. Tsunogai, S., Watanabe, S. & Sato, T. Is there a 'continental shelf pump' for the absorption of atmospheric CO_2? *Tellus B* **51**, 701–712 (1999).
56. Thomas, H., Bozec, Y., Elkalay, K. & de Baar, H. J. W. Enhanced open ocean storage of CO_2 from shelf sea pumping. *Science* **304**, 1005–1008 (2004).
57. Bates, N. R. Air–sea CO_2 fluxes and the continental shelf pump of carbon in the Chukchi Sea adjacent to the Arctic Ocean. *J. Geophys. Res.* **111**, C10013 (2006).
58. Laruelle, G. G. et al. Global multi-scale segmentation of continental and coastal waters from the watersheds to the continental margins. *Hydrol. Earth Syst. Sci.* **17**, 2029–2051 (2013).
59. Barrón, C. & Duarte, C. M. Dissolved organic carbon pools and export from the coastal ocean. *Global Biogeochem. Cycles* **29**, 1725–1738 (2015).
60. Luijendijk, E., Gleeson, T. & Moosdorf, N. Fresh groundwater discharge insignificant for the world's oceans but important for coastal ecosystems. *Nat. Commun.* **11**, 1260 (2020).
61. Chen, Z. L. & Lee, S. Y. Tidal flats as a significant carbon reservoir in global coastal ecosystems. *Front. Mar. Sci.* https://doi.org/10.3389/fmars.2022.900896 (2022).
62. Vonk, J. E. et al. Activation of old carbon by erosion of coastal and subsea permafrost in Arctic Siberia. *Nature* **489**, 137–140 (2012).
63. Terhaar, J., Lauerwald, R., Regnier, P., Gruber, N. & Bopp, L. Around one third of current Arctic Ocean primary production sustained by rivers and coastal erosion. *Nat. Commun.* **12**, 169 (2021).
64. Nielsen, D. M. et al. Increase in Arctic coastal erosion and its sensitivity to warming in the twenty-first century. *Nat. Clim. Change* **12**, 263–270 (2022).
65. Frey, K. E. et al. *Arctic Ocean Primary Productivity: The Response of Marine Algae to Climate Warming and Sea Ice Decline* NOAA Technical Report OAR ARC22-08 (NOAA, 2022).
66. Eyre, B. D. et al. Coral reefs will transition to net dissolving before end of century. *Science* **359**, 908–911 (2018).
67. O'Mara, N. A. & Dunne, J. P. Hot spots of carbon and alkalinity cycling in the coastal oceans. *Sci. Rep.* **9**, 4434 (2019).
68. Santos, F., Gomez-Gesteira, M., deCastro, M. & Alvarez, I. Differences in coastal and oceanic SST trends due to the strengthening of coastal upwelling along the Benguela current system. *Cont. Shelf Res.* **34**, 79–86 (2012).
69. Jacox, M. G., Moore, A. M., Edwards, C. A. & Fiechter, J. Spatially resolved upwelling in the California Current System and its connections to climate variability. *Geophys. Res. Lett.* **41**, 3189–3196 (2014).
70. Hallberg, R. Using a resolution function to regulate parameterizations of oceanic mesoscale eddy effects. *Ocean Model.* **72**, 92–103 (2013).
71. Moum, J. N., Nash, J. D. & Klymak, J. M. Small-scale processes in the coastal ocean. *Oceanography* **21**, 22–33 (2008).
72. Timko, P. G. et al. Assessment of shelf sea tides and tidal mixing fronts in a global ocean model. *Ocean Model.* **136**, 66–84 (2019).
73. Kossack, J., Mathis, M., Daewel, U., Zhang, Y. J. & Schrum, C. Barotropic and baroclinic tides increase primary production on the Northwest European Shelf. *Front. Mar. Sci.* https://doi.org/10.3389/fmars.2023.1206062 (2023).
74. Brearley, J. A., Moffat, C., Venables, H. J., Meredith, M. P. & Dinniman, M. S. The role of eddies and topography in the export of shelf waters from the West Antarctic Peninsula Shelf. *J. Geophys. Res. Oceans* **124**, 7718–7742 (2019).

75. Robinson, A. R., Brink, K. H., Ducklow, H. W., Jahnke, R. A. & Rothschild, B. J. in *The Sea: The Global Coastal Ocean: Multiscale Interdisciplinary Processes* Vol. 13 (eds Robinson, A. R. & Brink, K. H.) 3–35 (Harvard Univ. Press, 2005).
76. Heuzé, C. North Atlantic deep water formation and AMOC in CMIP5 models. *Ocean Sci.* **13**, 609–622 (2017).
77. Zheng, M. D. & Cao, L. Simulation of global ocean acidification and chemical habitats of shallow- and cold-water coral reefs. *Adv. Clim. Change Res.* **5**, 189–196 (2014).
78. Cotrim da Cunha, L., Buitenhuis, E. T., Quéré, C. L., Giraud, X. & Ludwig, W. Potential impact of changes in river nutrient supply on global ocean biogeochemistry. *Global Biogeochem. Cycles* **21**, GB4007 (2007).
79. Fréon, P., Barange, M. & Arístegui, J. Eastern Boundary Upwelling Ecosystems: integrative and comparative approaches. *Progr. Oceanogr.* **83**, 1–14 (2009).
80. Arrigo, K. R. & van Dijken, G. L. Continued increases in Arctic Ocean primary production. *Progr. Oceanogr.* **136**, 60–70 (2015).
81. Jiang, L. Q., Carter, B. R., Feely, R. A., Lauvset, S. K. & Olsen, A. Surface ocean pH and buffer capacity: past, present and future. *Sci. Rep.* **9**, 18624 (2019).
82. Westberry, T. K., Silsbe, G. M. & Behrenfeld, M. J. Gross and net primary production in the global ocean: an ocean color remote sensing perspective. *Earth Sci. Rev.* **237**, 104322 (2023).
83. Mathis, M. ICON-Coast model output for a study on increasing CO_2 uptake of the coastal ocean. *Zenodo* https://doi.org/10.5281/zenodo.7964987 (2023).
84. Mathis, M. ICON-Coast source code and primary model output. *Zenodo* https://doi.org/10.5281/zenodo.6630353 (2022).

Acknowledgements

This work contributed to the subproject 'A5 - The Land–Ocean Transition Zone' of Germany's Excellence Strategy EXC 2037 'CLICCS - Climate, Climatic Change, and Society' with project no. 390683824, funded by the Deutsche Forschungsgemeinschaft (DFG, German Research Foundation). Computational resources were made available by the German Climate Computing Center (DKRZ) through support from the German Federal Ministry of Education and Research (BMBF). T.I. was supported by the European Union's Horizon 2020 research and innovation programme under grant agreement no. 101003536 (ESM2025 - Earth System Models for the Future). Open-access funding was provided by Helmholtz-Zentrum hereon GmbH.

Author contributions

M.M., T.I. and C.S. planned and coordinated the study and designed the model experiments. M.M. and S.H. provided forcing data. M.M. contributed to the model development and performed the experiments. M.M., D.M.N. and F.L. analysed the model output and discussed the interpretation of the results. M.M. wrote the manuscript with contributions from all co-authors.

Funding

Open access funding provided by Helmholtz-Zentrum hereon GmbH (4216).

Competing interests

The authors declare no competing interests.

Additional information

Extended data is available for this paper at https://doi.org/10.1038/s41558-024-01956-w.

Supplementary information The online version contains supplementary material available at https://doi.org/10.1038/s41558-024-01956-w.

Correspondence and requests for materials should be addressed to Moritz Mathis.

Peer review information *Nature Climate Change* thanks Laure Resplandy, Tim Rixen and Raphaël Savelli for their contribution to the peer review of this work.

https://doi.org/10.1038/s41558-024-01956-w

Extended Data Table 1 | Coastal ocean carbon fluxes

Coastal ocean carbon budget	*ctrl* gC m^{-2} yr^{-1}	*woriv* gC m^{-2} yr^{-1}	*hist* gC m^{-2} yr^{-1}	Δ *woriv* gC m^{-2} yr^{-1}	Δ *hist* gC m^{-2} yr^{-1}
NPP	145	150	166	**+5**	**+21**
OC remin	127.1	131.3	143.7	**+4.2**	**+16.6**
Export fluxes:					
OC advective	+22.1	+23.1	+25.9	**+1.0**	**+3.8**
IC advective	-3.3	-1.4	-4.1	**+1.9**	**-0.8**
OC sediment	+6.4	+6.2	+7.0	**-0.2**	**+0.6**
IC sediment	+0.1	+0.1	+0.3	-	**+0.2**
FCO2	-3.1	-6.9	-7.9	**-3.8**	**-4.8**
OC rivers	-10.6	-10.6	-10.6	-	-
IC rivers	-12.2	-12.2	-12.2	-	-
Storage fluxes:					
IC stock	+0.6	+1.7	+1.6	**+1.1**	**+1.0**
OC stock	-	-	-	-	-

Carbon budget of the global coastal ocean, derived from experiments *ctrl*, *woriv* and *hist* for the period 1991-2010, as well as change signals Δ *woriv* (*woriv* minus *ctrl*) and Δ *hist* (*hist* minus *ctrl*). Values are rounded to one digit after the decimal point, and thus excluded if smaller than 0.05. Positive exchange fluxes correspond to net export fluxes from the shelf to the open ocean, sediment or atmosphere. Positive storage fluxes correspond to net accumulation rates in the water column. Change signals given in bold are statistically significant at the 95% confidence level, based on a 2-sided *t*-test. NPP: net primary production; OC remin: remineralization of total organic carbon in continental shelf waters; OC/IC advective: net export of total organic/inorganic carbon to the open ocean via advective transport; OC/IC sediment: net deposition of total organic/inorganic carbon in shelf sediments; FCO_2: net CO_2 flux at the sea surface (positive from the ocean to the atmosphere); OC/IC rivers: total organic/inorganic carbon supply via river discharge (trends in riverine carbon inputs are not considered; see Methods section); OC/IC stock: total storage of organic/inorganic carbon in shelf waters (the IC stock increase of *ctrl* is due to model drift). Further distinctions into particulate and dissolved carbon fluxes can be found in Fig. 3.

https://doi.org/10.1038/s41558-024-01956-w

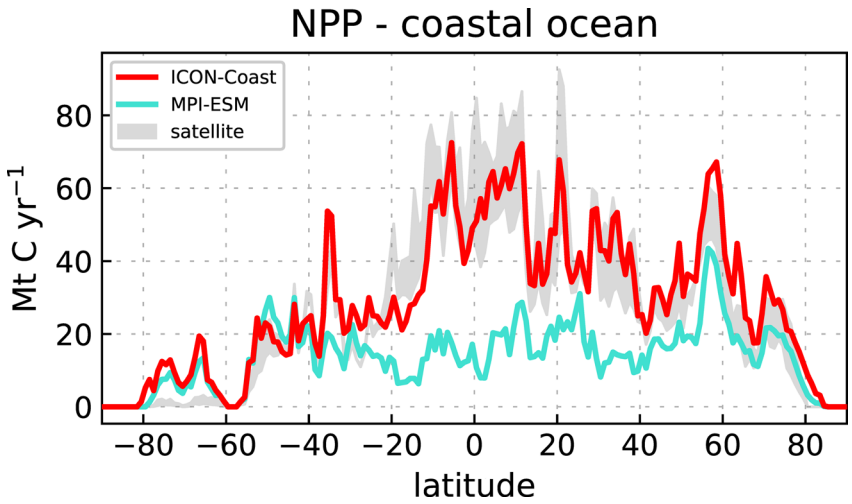

Extended Data Fig. 1 | Latitudinal distribution of marine primary production. Comparison of zonally integrated net primary production (per 1° latitudinal band) in the coastal ocean between ICON-Coast, the global Earth system model MPI-ESM-LR, and the range of two satellite-based products (MODIS-CAFE and VIIRS-CBPM). Differences are less pronounced in high latitudes as here NPP is strongly influenced by light availability and sea ice cover, and riverine nutrient inputs (which are neglected by MPI-ESM) are much lower than in low latitudes.

https://doi.org/10.1038/s41558-024-01956-w

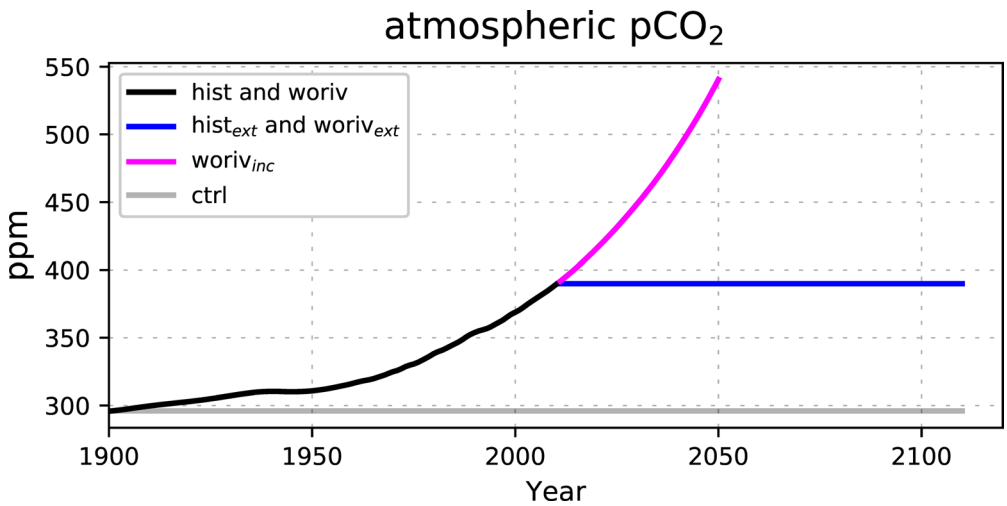

Extended Data Fig. 2 | Atmospheric pCO_2 in model experiments. Overview of prescribed atmospheric pCO_2 used in the different model experiments. Black: historical pCO_2 record (used for *hist* and *woriv*); magenta: hypothetical pCO_2 according to emission scenario RCP8.5 (used for $hist_{inc}$); blue: constant pCO_2 of the year 2010 (used for $hist_{ext}$ and $woriv_{ext}$); grey: constant pCO_2 of the year 1900 (used for *ctrl*). Further information on the forcing conditions is given in Table 1.

https://doi.org/10.1038/s41558-024-01956-w

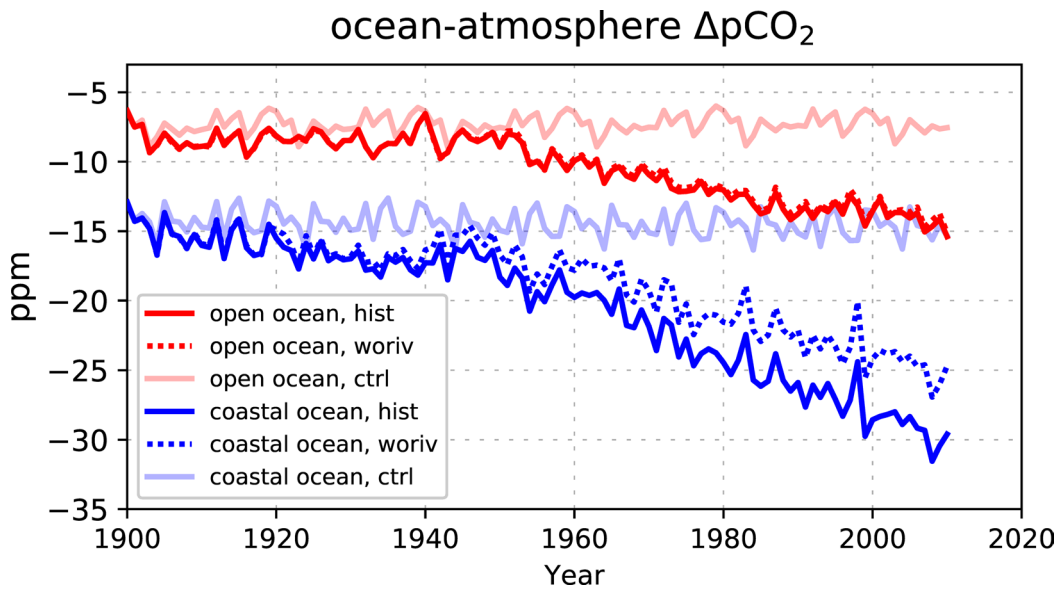

Extended Data Fig. 3 | ΔpCO_2 in the open and coastal ocean. Time series of simulated ocean-atmosphere ΔpCO_2 for the open (red) and coastal (blue) ocean. Negative ΔpCO_2 indicates ocean undersaturation. *hist*: historical hindcast, *woriv*: same as *hist* but without increasing nutrient loads from land, *ctrl*: control run with constant forcing.

https://doi.org/10.1038/s41558-024-01956-w

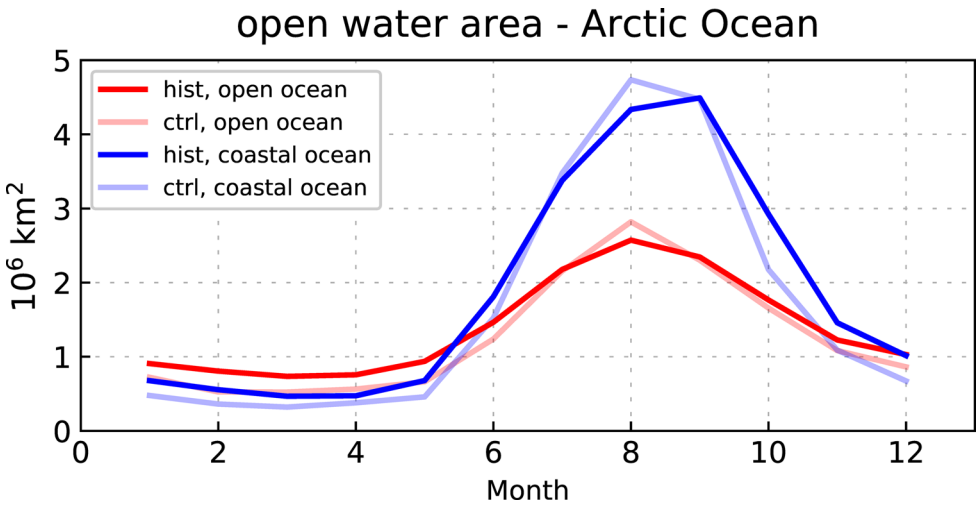

Extended Data Fig. 4 | Arctic open-water area. Seasonal cycle of simulated open-water area in the Arctic Ocean (north of 66°N), separated for the open (red) and coastal (blue) ocean. Grid cells are considered as open-water condition if their areal sea ice cover is less than 20%.

https://doi.org/10.1038/s41558-024-01956-w

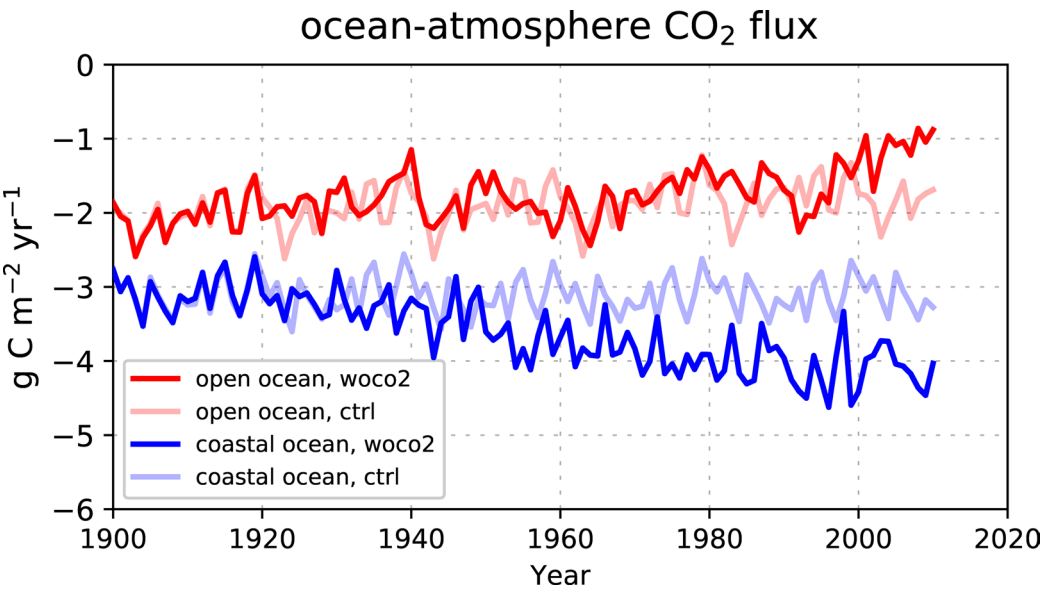

Extended Data Fig. 5 | Omitting increasing atmospheric pCO_2. Time series of simulated ocean-atmosphere CO_2 flux for the open (red) and coastal (blue) ocean. Negative values indicate ocean CO_2 uptake. *woco*$_2$: same as the hindcast *hist* but without increasing atmospheric pCO_2, *ctrl*: control run with constant forcing.

https://doi.org/10.1038/s41558-024-01956-w

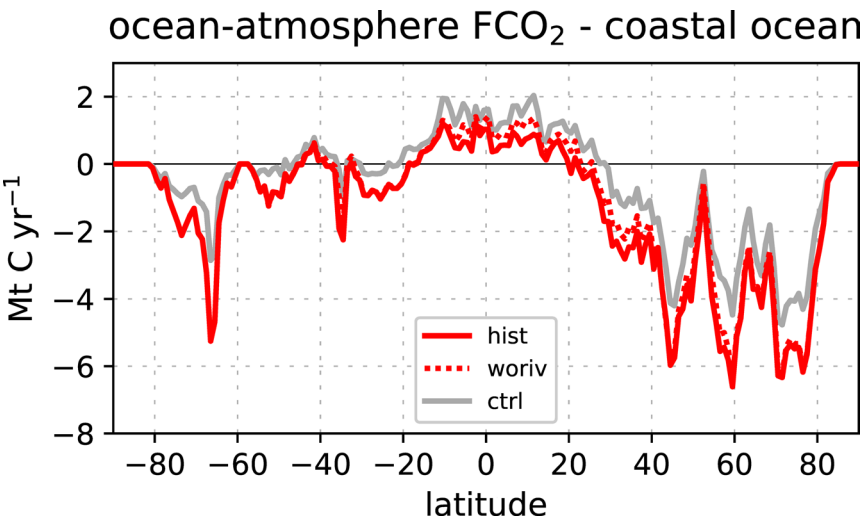

Extended Data Fig. 6 | Latitudinal distribution of CO_2 surface flux. Zonally integrated CO_2 surface flux (per 1° latitudinal band) in the coastal ocean, shown for the control run (grey) as well as means over 1991-2010 of the hindcast *hist* (solid red) and experiment *woriv* where increasing nutrient inputs from land were excluded (dashed red). Positive fluxes indicate CO_2 outgassing.

https://doi.org/10.1038/s41558-024-01956-w

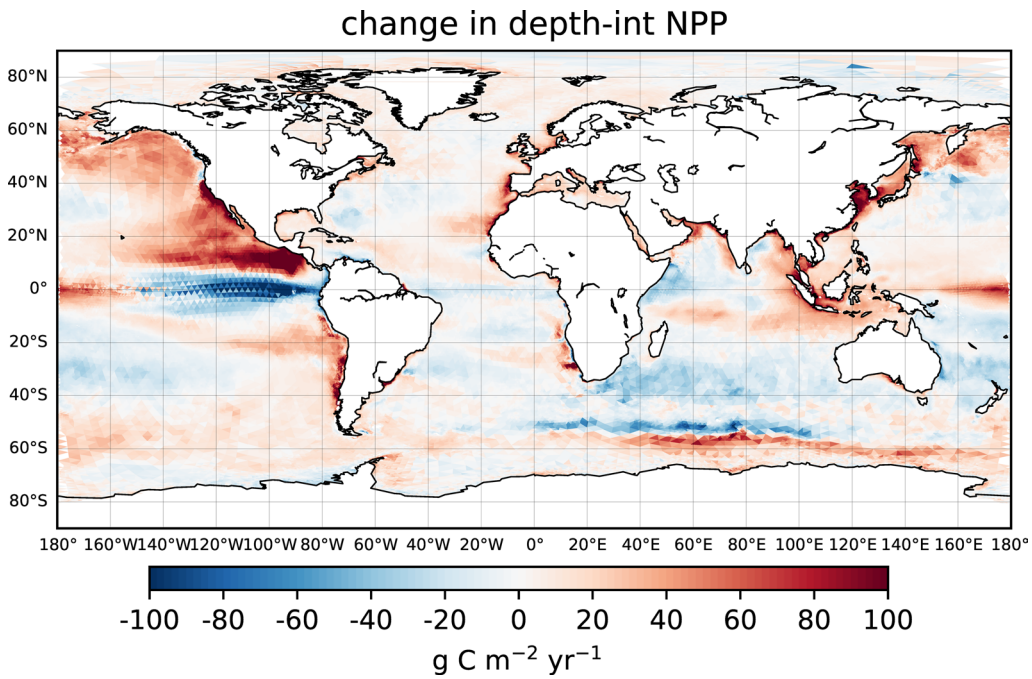

Extended Data Fig. 7 | Changes in marine primary production. Simulated change signal of depth-integrated net primary production during the 20th century (experiment *hist*).